Bulletin of the Seismological Society of America, Vol. 109, No. 6, pp. 2159–2167, December 2019, doi: 10.1785/0120180128

Beyond Backslip: Improvement of Earthquake Simulators from New Hybrid Loading Conditions

by Bruce E. Shaw

Abstract A standard approach to loading earthquake simulators involving complex fault system geometries is the backslip method, by which fault-slip rates are specified and stressing rates giving the specified slip rates are calculated and imposed on the system. This often results in singularities in stressing rate at fault boundaries, and unrealistic hypocenters of events associated with these singularities. We present a new generalized hybrid loading method that combines the ability to drive faults at desired slip rates while loading with more regularized stressing rates, allowing faults to slip in a more natural way. The resulting behavior shows improvement in the depth dependence of seismicity, the distribution of sizes of events, and the depth dependence of slip. We discuss as well the physical implications of the new type of loading.

Introduction

A variety of earthquake simulators have been developed that aim to simulate sequences of events on complex natural fault systems (Robinson *et al.*, 2011; Pollitz, 2012; Sachs *et al.*, 2012; Tullis *et al.*, 2012; Ward, 2012). To get faults to slip at observed fault-slip rates, the standard approach is to load faults under backslip conditions, whereby fault-slip rates are specified everywhere, and then based on static stress interactions between fault elements, stressing rates that would reproduce the long-term slip rates are calculated and then imposed on the fault system (Savage, 1983). This gives the ability to drive the faults at arbitrary slip rates. It also gives the ability to simulate earthquakes on the faults for very long lengths of time, as stressing rates and slip rates are calculated to be compatible with the fault system geometry by construction. One difficulty with the method is that slip rates need to be specified everywhere, so assumptions must be made about slip in areas that cannot be directly measured such as at depth. In the absence of information, simplified profiles are often assumed such as constant rates along faults and with depth. A complication arising from this approach is that these kinds of assumptions can lead to singular stressing rates at fault edges. This manifests itself in behaviors in the simulators that appear unrealistic when compared with observations, including a band of intense model hypocenters on the fault boundaries.

An alternative loading approach has been to load faults remotely, having more uniform stressing rates drive faults, and letting fault-slip rates respond in a self-organizing way (Shaw *et al.*, 2015). This has the virtue of not needing to know the slip rates—they emerge from the simulation. This works well in model systems in which no particular slip rates are desired on specific faults but becomes less useful when applied to specific fault systems with target slip rates, as small details in fault geometry can impact self-organizing fault-slip rates—details that are not knowable at depth—and self-organizing rates can be substantially different from observed rates. In addition, stresses can build up in the system, so very long timescale simulations are difficult to run and steady state hard to achieve.

In this article, we introduce a new hybrid approach that combines the virtues of both types of methods, and gives as a consequence improvements in simulator behaviors. With our new hybrid method, we are able to drive faults at targeted slip rates, not only in a long-term steady state way but also load in a gentle or less singular way. Improvements in the depth dependence of seismicity, distributions of sizes of events, and depth dependence of slip arise in using the new method. An application of this new hybrid loading simulator to seismic hazard estimates in California, showing replication of estimated hazard across California compared with the leading statistical model, was published last year ahead of this article (Shaw *et al.*, 2018), using the loading techniques developed and presented here.

The article is organized as follows. We begin by presenting the model and the new loading method. The method is more general than the specific model we apply it to, but for completeness in understanding the setting in which the loading method is applied, and the results, we also discuss the model. Next, we present results of the new loading applied to the model. We compare it to more standard backslip loading methods, to show improvement in a number of behaviors. We end with some discussion and conclusions.

The Model

The core engine of the model is the RSQSim platform developed by Dieterich and Richards-Dinger (2010). It is a

boundary element model using three key approximations. First, elements interact with quasi-static elastic interactions, so dynamic stresses are neglected. Here, elements are small pieces of faults, treated as Okada-type dislocations with constant slip across these small numerical patches, and typically triangular-shaped elements (Gimbutas *et al.*, 2012) so faults having nonplanar surfaces can be tiled without gaps. Second, rate-and-state frictional behavior is simplified into a three-regime system in which elements are either stuck, nucleating, or sliding dynamically. Third, during dynamic sliding the slip rate is fixed at a constant sliding rate. These approximations allow for analytic treatments of rate-and-state behaviors in different sliding regimes, and a tremendous speedup computationally over inertial (Bouchon and Streiff, 1997; Andrews, 1999; Harris and Day, 1999; Aagaard *et al.*, 2004; Day *et al.*, 2005; Dalguer and Day, 2007; Harris *et al.*, 2009; Lapusta and Liu, 2009) and traditional quasi-static methods (Ben-Zion and Rice, 1997; Ward, 2000). This speedup occurs through the use of analytic expressions for the updating in different sliding regions that relieves the need for continuous updating, and instead only updates when elements change from one sliding state to another, thereby allowing for efficient adaptive timesteps. This feature also illuminates why only quasi-static elastic interactions are considered, as skirting the Courant condition related to inertial waves is an essential feature for allowing timesteps longer than waves propagating over grid scale elements would otherwise permit. Richards-Dinger and Dieterich (2012) presented a number of favorable comparisons of this model with fully dynamic simulations and observations, though they are, of course, not equivalent. Importantly, the main features of the rate-and-state equations are preserved, leading to delayed nucleation and other effects in which clustering of events arises naturally and appears realistic when compared with earthquake observations (Richards-Dinger and Dieterich, 2012; Shaw *et al.*, 2015). These include comparisons with repeat times in repeating small events following a stress step and Omori-law aftershocks (Richards-Dinger and Dieterich, 2012), and spatial distributions of aftershocks and aftershock productivity on more complex fault systems (Shaw *et al.*, 2015).

Dieterich and Richards-Dinger (Dieterich and Richards-Dinger, 2010; Richards-Dinger and Dieterich, 2012) discussed the model in much more detail. At a basic level, fault elements interact through static elastic interactions. They slide based on stress and frictional criteria. They are loaded by stressing rates. They slide fast when shear stresses are high enough relative to normal stress and friction. During fast sliding, stress redistribution occurs rapidly and this can recruit other elements to participate in the same event. Otherwise, between events the system is slowly loaded. Long-term slip rates on faults are used in initial calculations to help set the slow tectonic loading stresses between events.

Separating out the different kinds of ingredients in the model helps illuminate how what we are doing differs from prior efforts. There are three main types of parameterized ingredients to the model. One concern is the fault system and its geometry. The second concerns how these faults are loaded. The third concerns how events occur in the model. It is this middle second loading set that we will be doing differently in this article. But to set the stage, we briefly mention them all here.

Fault geometry parameters determine the collective set of elements, giving their locations. We automate this procedure in generating the elements. Two types of data enter in to the fault geometry process. One is the target set of faults we are aiming to numerically approximate. The second set is numerical parameters allowing for approximations of this target set of faults. These numerical parameters include target element sizes and shapes, and how to compromise these target shapes to tile and fit larger nonplanar fault surfaces and networks of these surfaces. Having an automated process allows for parameter sensitivity studies. Robustness of behaviors to parameter choices is examined to establish genericness of behaviors.

Rupture parameters impacting how events occur include rate-and-state friction parameters and sets of other associated numerical parameters that determine how events slip and evolve based on stress criteria. These parameters include parameters determining how individual elements begin to slip, begin to slip seismically, and stop sliding. Elements slide based on frictional criteria, which combines shear stress, normal stress, and frictional terms based on rate-and-state friction (Dieterich and Richards-Dinger, 2010).

Loading parameters determine how slow steady tectonic loading drives the fault system and builds up stresses that eventually are relieved by seismic events in the model. This is where the innovations we discuss in this article lie. The most commonly used method of loading complex fall systems is the method of backslip loading. Based on ideas going back to Savage (1983), one specifies the target long-term slip rates at points along faults, and then, fixing slip rates at these target rates calculates through the elastic stiffness interactions between elements the resulting collective long-term stressing rates which arise. By imposing these long-term stress rates, one then recovers in the long run the long-term slip rates. An advantage of this method is it gives long-term slip rates that match the desired target slip rates even for very complex geometries. A disadvantage is that it can lead to strongly heterogeneous, even singular stressing rates in some places, depending on the fault geometry and imposed target slip rates. More problematically, these strongly heterogeneous and singular stressing rates can have a strongly distorting impact on the behaviors of the models. It is the purpose of this article to introduce improved ways of loading that retain features of maintaining target slip rates while generating associated stressing rates that no longer overwhelm behaviors and allow more realistic self-organizing behaviors.

Hybrid Loading

The method of hybrid loading is meant to tie faults to target long-term slip rates, but then load them gently in a way

that does not overforce them to slip in ways they generally would not (e.g., discontinuously along the fault), as they are self-organizing systems ultimately (Shaw, 2004). Traditional backslip methods that load at a constant slip rate along a fault and to the base of the seismogenic depth create stressing rate singularities at the base and ends, and generate many small events at those edges that try to fill in the imposed long-term slip-rate profile. This lighting up around the bottom and edges of faults is not typically seen in hypocentral distributions. Here, we aim to recreate the long-term slip rates along the bulk of the fault but add gentler stress-rate loading to accomplish this. The procedure, applied to each individual fault in a fault system, is discussed later. A fault is an extended surface along strike and with depth across which slip discontinuities develop. It is a 2D (not necessarily planar) object embedded in a 3D elastic half-space. The specified target strike and dip and rake can all vary along a fault. Faults can be very complicated geometrical objects individually, and even more so as a collection of faults—a fault system. Faults do not need to be planar or isolated for the following procedure to work. Faults are represented in a discretized way in the simulator by tiling with connected triangular elements, which allow for nonplanar surfaces. The new loading procedure is as follows.

1. Begin with a target slip rate. Typically, this is taken to be a constant along strike and with depth, but if further information is available to modify this, other slip profiles can be used.
2. Calculate what the stressing rates would be for the fault system loaded in backslip mode with this slip-rate profile.
3. Smooth and modify the backslip-estimated stressing rates. This is done with a series of filters.
   a. Add upper and lower unstressed layers to represent the nonseismogenic layers. On the top Z_1 km and bottom Z_2 km in depth the shear stressing rate is zeroed out. This is done to load the fault and as a consequence cause events to nucleate in the seismogenic middle zone. A physical justification for the lower stressing rate in the upper layer is the lower modulus. In the lower layer, it is higher temperature creep relaxation processes. The effect in the simulator is to improve the depth dependence of the hypocenters.
   b. A correction factor increasing the overall stressing rate on the fault to make up for zeroing the stressing rate on the top and bottom edges is then applied to match the slip rate on the faults. A first-order estimate of this correction factor would be $H/(H - Z_1 - Z_2)$, in which H is the fault depth. This would be all that is needed in the case of loading with initial constant stressing rate with depth, but typical slip profiles such as initially constant slip rate with depth have nonconstant stressing rates with depth, and additional correction factors may be needed. For a constant slip profile with depth, there are higher stressing rates on the bottom, so a higher correction factor is needed. For the case $H = 18$, $Z_1 = 2$, $Z_2 = 4$ km with slip constant with depth we use in the model we discuss later, a factor of 1.2 was seen empirically to give a good match to slip rates. Using this added correction, we apply everywhere an overall multiplicative factor $1.2H/(H - Z_1 - Z_2)$.
   c. On the vertical edges Z_3 km wide we take the median stressing rate for the fault and apply it to the sides. We also use the same zeroing of stresses on the top and bottom as in the step (b). This gets rid of stress singularities at the fault edges and applies a typical (median) stressing rate for that fault to the vertical edges.
4. Using this new filtered modified stressing rate, run for a long time (tens of thousands of years).
5. Measure accumulated slip at each element over this long run and divide by time to get slip rates at each element along faults.
6. Use these new empirical long-term fault-slip rates, varying spatially along faults and with depth but constant in time, as input slip rates to calculate backslip loading. This is the new backslip-from-stress loading mode. This empirical slip rate can be used for different rupture parameters than it was generated under because it only depends on the cumulative long-term slip, not the individual slip-event increments.

Figure 1 illustrates the method with a single rectangular fault that breaks the surface. We can apply it to much more complex faults, but this simple case illustrates the method. Figure 1a shows the stressing rates calculated with backslip when imposing constant slip rates on the rectangular fault. Figure 1b shows the modified stressing rates derived from the above-mentioned procedure applied to the backslip rates in Figure 1a. We see the three length scales impacting the model, one at the top and one at the bottom over which the stressing rates are zeroed, and one on both sides where a median stressing rate is used. We also see that the stressing rates are raised somewhat on the interior to make up for the zeroing of the stressing rates on the top and bottom.

Figure 2 shows the method applied to the California fault system. This fault system is derived from the third Uniform California Earthquake Rupture Forecast (UCERF3) fault system (Field *et al.*, 2014). The UCERF3 fault system consists of fault subsections and slip rates and rakes on those subsections. The slip rates come from the UCERF3 geological model, which while being the most closely tied to geological observations of the various UCERF3 versions, is itself a model, as geological observations are not dense enough to determine slip rates at the spatial densities needed (Dawson and Weldon, 2013; Field *et al.*, 2014). Our simulator representation is not precisely the UCERF3 fault system, which consists of a series of rectangular fault subsections, but rather uses these as target geometries that are smoothed into a more continuous set of faults. The simulator smoothing of this target UCERF3 model is important

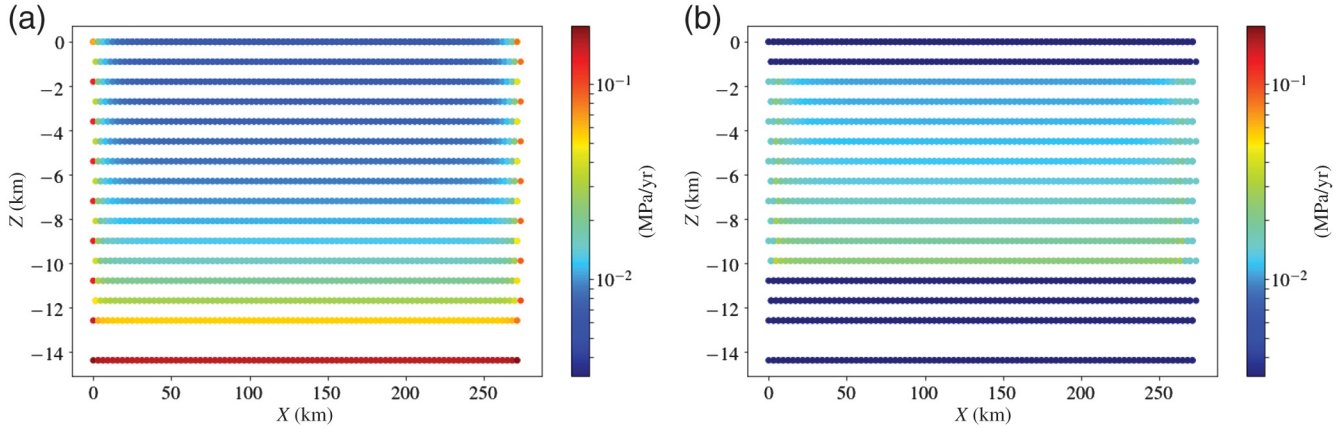

Figure 1. Loading geometry for backslip and new hybrid method illustrated on a planar rectangular fault. The view is from the side of a vertical strike-slip fault. The top is a free surface, and there is no slip beyond the sides and bottom of the fault. Color is stressing rate in units of MPa/yr, with a lower bound cutoff. (a) Stressing rate calculated from backslip method having fault slide at uniform slip rate. Grid resolution is 1.8 km, which sets the upper stressing rate limit. Note the highly stressed red regions on the fault edges on the bottom and sides (though not at the free surface top). The vertical axis is exaggerated relative to the horizontal axis. (b) Modified stressing rate from new method. The upper $Z_1 = 2$ km and lower $Z_2 = 4$ km parts of the fault have zero stressing rates, whereas the middle seismogenic zone has an increased rate to make up for the zeroing of stressing rate on the top and bottom. On the $Z_3 = 5$ km sides of the fault, a median stressing rate is applied. These three boundaries can be seen in this panel.

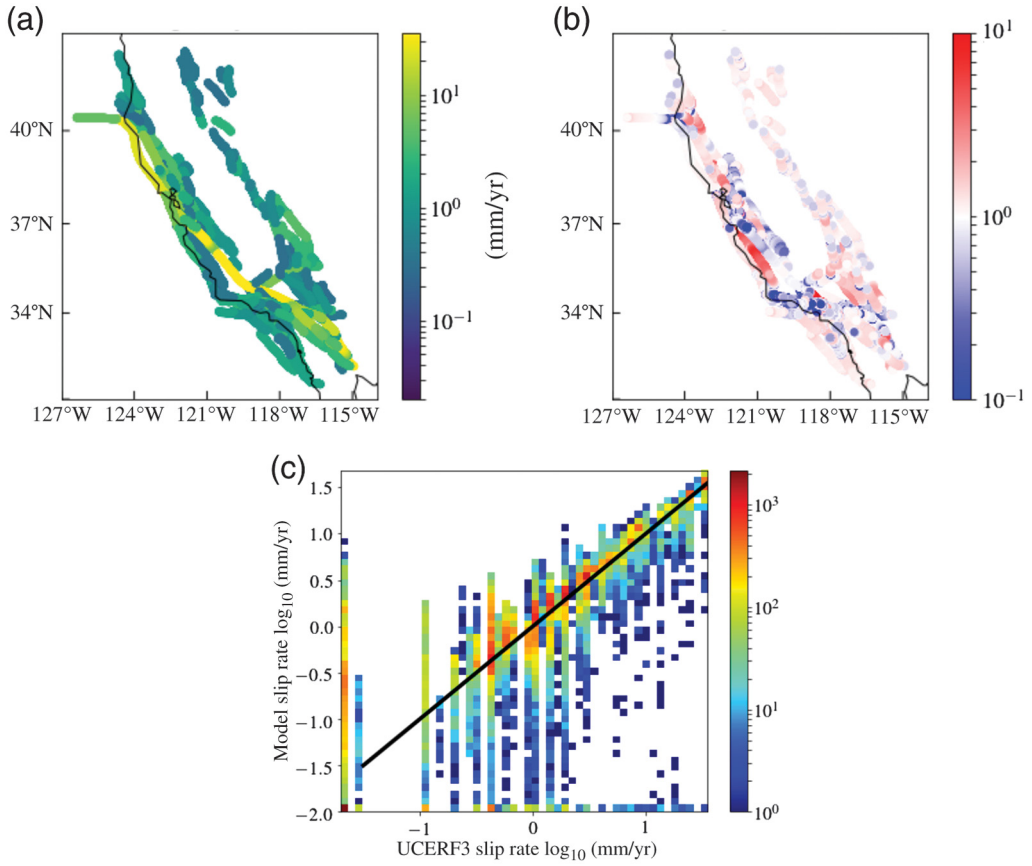

Figure 2. Demonstration on the California fault system that the method works in recreating target slip rates. (a) Target the third Uniform California Earthquake Rupture Forecast (UCERF3) geological model slip rates. Units are in mm/yr slip rates. (b) Ratio of simulated slip rates under hybrid loading relative to target rates. Units are a dimensionless ratio. Ratio is shown for mid-seismogenic depths, where model aims to match target rates. Only faults above a minimum slip rate (0.2 mm/yr) are shown. (c) 2D histogram of hybrid model elements versus target UCERF3 slip rates at mid-seismogenic depths. Slip rates are $\log_{10}$ in mm/yr. Black line shows equal rates. Color shows number of states in histogram bins. Note that the faster moving model faults, those above around 1 mm/yr ($\log_{10} = 0$), most accurately track the target fault-slip rates, indicated by the better fit of the dense orange and red parts of the histogram to the black line in the upper right quadrant of (c).

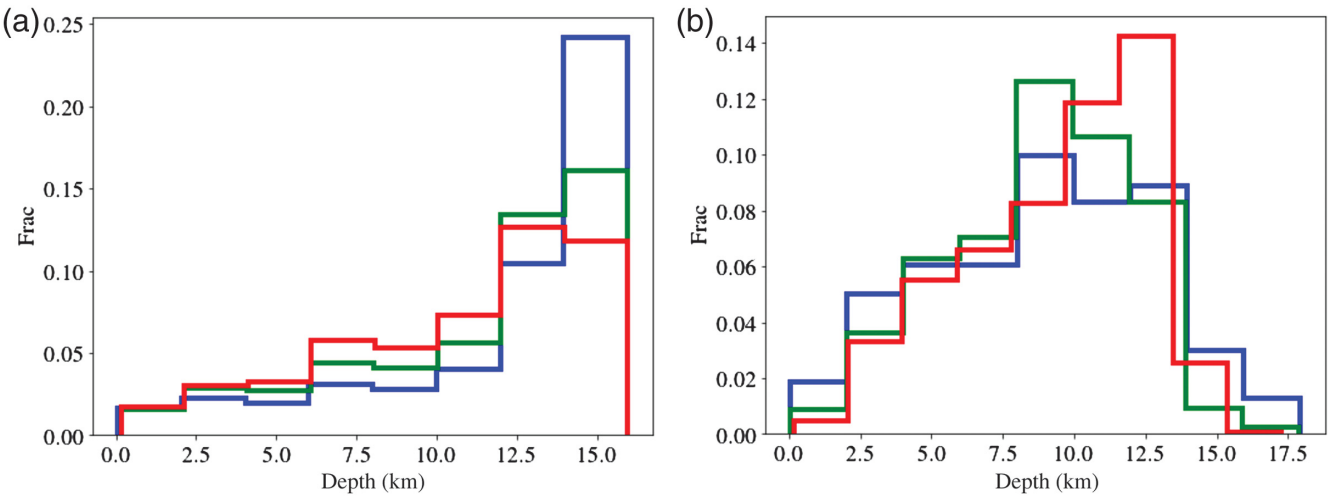

Figure 3. Depth distribution of seismicity. (a) Backslip loaded; (b) hybrid loaded. Colors represent different magnitude ranges, with **M** 5 ($5 \leq \mathbf{M} < 6$) in blue, **M** 6 in green, and **M** 7+ ($7 < \mathbf{M}$) in red. Note the traditional backslip loaded model has an intense band of hypocenters on the bottom of the fault. For the hybrid loading, in contrast, most of the hypocenters occur in the seismogenic layer. Note also the feature of a higher proportion of the largest events initiating deeper relative to the moderate-size events in the hybrid loading model, something that emerges in the model.

because the rectangular UCERF3 fault representation has many discontinuities along strike and with depth for neighboring changes in strike, dip, and dip direction, and rectangular tilings are difficult to use to represent continuous nonplanar surfaces. We therefore tile surfaces using triangles, and smooth to aim to reduce artificial discontinuities introduced by the rectangular representation. We also do this with and aim for a more regular triangular grid so as to minimize element discretization effects. Thus, we approximate in a more continuous way that UCERF3 fault geometry, which is itself an approximation of the real system. Figure 2a shows the target geological slip rates in the UCERF3 model. Figure 2b shows the ratio of the simulated slip rates emerging from the model under the new hybrid loading conditions relative to the target rates, plotted at mid-seismogenic depths where the model aims to match the targeted slip rates. We see we are in general achieving this goal. There are, of course, some differences at the edges of faults. Also, we do not plot the very slow moving faults, those with slip rates <0.2 mm/yr, to initially focus attention on the accuracy of the most important faults. To probe the differences further and include the slower moving faults, Figure 2c shows a 2D histogram of the $\log_{10}$ slip-rate values at mid-seismogenic depths along faults versus the target rates. We see the model does best on the faster moving faults. We also see there are some edge cases in which the target slip rates are much higher, and the hybrid loaded faults are barely slipping, and conversely some target slower moving fault cases in which the hybrid loading slip rates are much faster than the slow target rates. The cases in which the target rates are much higher at fault ends are an expected feature. The converse case in which target slower moving faults are slipping much faster represent an inaccuracy in the simplest version of the hybrid method we present earlier, in that the model does aim to match the target slip rates but is missing it due to fault interactions. As can be seen in the map view in Figure 2b, these are limited areas, and mainly involve complex overlapping fault regions. If greater fidelity to the target slip rates is desired, additional modifications to the slip-rate profiles can be made, adding further steps to the method outlined earlier. In the interest of simplicity, to see how behaviors are being impacted by this first-order loading modifications, we accept for now the modest inaccuracies and continue with this baseline hybrid loading.

Impacts on Behaviors

With the new loading method, we find improvements in a number of behaviors compared with observations, including the depth dependence of seismicity, the distribution of sizes of events, and the depth dependence of slip. Here, we focus on comparing behaviors in the model under hybrid loading as compared with traditional backslip loading, the discussion referenced relative to the observed earthquake behaviors. Thus, we just present model data but are concerned with how realistic it is.

Depth of Seismicity

One behavior improvement with hybrid loading is the depth distribution of seismicity. With traditional backslip, one finds an excess of hypocenters near the edges of faults. This is due to the singular stressing rates arising from typically imposed slip profiles. Figure 3 shows the hypocenters with the new hybrid loading conditions, contrasted with those under a more traditional backslip loading. We see a vastly improved depth distribution with hypocenters now concentrated mainly at seismogenic depths (Nazareth and Hauksson, 2004). Interestingly, we also see a feature often

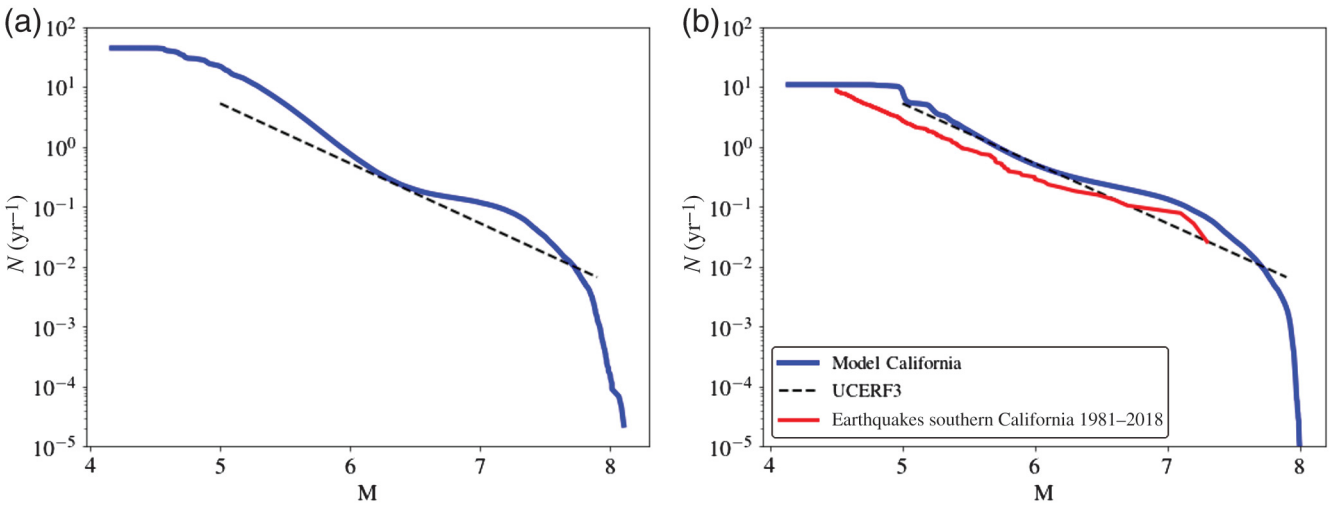

Figure 4. Magnitude distribution of seismicity. The cumulative rate of events per year above a given magnitude is plotted against magnitude. The dashed line shows the best estimate for the observed rate of **M** 5+ events on the UCERF3 faults, extrapolated with a *b*-value of one. The blue line shows the model California fault system events. (a) Backslip loaded; (b) hybrid loaded. The red line shows observed earthquake in southern California from the Southern California Earthquake Center Data Center catalog (Hauksson *et al.*, 2012) for 1981–2018 for comparison. Although the correspondence is very good in this case, other magnitude distributions can be found depending on model parameters, so this quantitative agreement is not a completely generic feature but rather one that can be examined and is important to compare against.

discussed in the literature of having larger event hypocenters preferentially initiating deeper relative to smaller event hypocenters arising in the hybrid loaded model (Mai *et al.*, 2005; Manighetti *et al.*, 2005). The detailed depth distribution has some dependence on the buffer length scales Z_1 and Z_2, imposed at the top and bottom, as stressing rates associated with constant slip with depth do have some depth dependence, so now zeroing the edges and reapportioning this stressing rate to seismogenic depth does depend on the full H, Z_1, Z_2, and slip profile assumptions. Nevertheless, choosing values for these parameters associated with seismogenic depths as done in Figure 3b gives behavior that compares well with observations. Furthermore, the dependence is not overly sensitive, and depends smoothly and continuously on these parameters, with hypocenters concentrated in the seismogenic band of depths from the Z_1 to $H - Z_2$ depth range. We use the dearth of hypocenters in the upper few kilometers (Marone and Scholz, 1988) to set Z_1, and the drop-off in hypocenters at the bottom to constrain the lower seismogenic depth $H - Z_2$. On the sides of faults, we set the Z_3 scale lengths to be a fraction of seismogenic depths $H - Z_1 - Z_2$. The results are not sensitive to Z_3; we choose a value based on being at least a few times the grid scale and smaller than the seismogenic depth so faults can self-organize the slip taper at fault ends based on stress continuity (Cowie and Scholz, 1992; Shaw, 2004). Larger values of Z_3 could also be used, but a more detailed comparison of slip profiles against geological observations as opposed to just target slip rates would be called for as more of the fault is left to self-organize. Such comparisons have shown promise in smaller regional efforts (Marshall *et al.*, 2008) but is beyond the scope of our initial statewide model here.

Distribution of Sizes of Events

A second behavior impacted by the hybrid loading is the distribution of sizes of events. We find a characteristic distribution of an excess of large events under both the traditional backslip and new hybrid loading, but the distribution of smaller events appears more realistic under the hybrid loading conditions, with a Gutenberg–Richter *b*-value much closer to unity. Figure 4 shows the cumulative distribution of sizes of events above a given magnitude on the UCERF3 fault system for the hybrid contrasted with traditional backslip loading. We see an overly steep *b*-value of small events in the backslip loading case in Figure 4a, in contrast with a more reasonable fall-off in small events for the hybrid case in Figure 4b. The smallest event sizes are set by the element size combined with the loading. The smallest elements on the fault boundary coincide with the singular boundary loading to increase the rate of the very smallest events in the traditionally backslip loaded model. Reducing the loading on the fault edges reduces these smallest events. The reduction of these events in the hybrid model is an additional advantage of the hybrid model. A further feature of the hybrid model is that not only does the *b*-value slope look reasonable, but the overall rate of moderate-size events on the faults, the *a*-value in the Gutenberg–Richter distribution also looks reasonable. The dashed line shows the best estimate of the historically observed rate of **M** 5+ events on the UCERF3 faults. This is obtained from the preferred value emerging from the UCERF3 estimates, taking the highest weighted branch considered to best match the instrumental and historical record for rate of **M** 5+ events, and multiplying that value by two-thirds to account for the fraction of events in UCERF3 that are on fault (with one-third occurring off

faults, which are not being modeled in the simulator; Field *et al.*, 2014). There are of course uncertainties in these values, which is why there are different branches for estimates of these values in the UCERF3 model. The high and lower values on the other branches considered in UCERF3 are a factor of 1.2 higher and lower than this preferred value, giving a sense of the range of uncertainties in the estimates of these values based on the finite observed catalog. As a further check on the consistency of the model behaviors with observations, in Figure 4b we plot the distribution of sizes of earthquakes in the southern California catalog from 1981 to 2018, shown with a red line. This comes from the catalog from the onset of the digital era in 1981 through the most recent year. A more complete comparison would include the whole state, but we are missing many active offshore faults in the upper Cascadia plate above the Mendocino triple junction, and very productive sequences of **M** 6 events in the Mammoth lakes area associated with volcanic hotspots also distort the catalog. To avoid additional complications, and because a full statistical analysis of the comparison is beyond the scope of this article, we opt for the simplicity of using this well-controlled well-studied catalog (Hauksson *et al.*, 2012) as a basic consistency check. Intriguingly, the characteristic bump in the model appears quite compatible with the observations. Going beyond this qualitative comparison will require a full statistical analysis accounting for finite numbers in the observed catalog, on-fault versus off-fault events, incompletely overlapping geophysical regions, and for robustness of model results. This is planned for future work. One caveat on the comparison of the distribution of sizes to observations is that in some recent models aiming to develop an even smoother representation of the UCERF3 faults, we find dependence of the distribution of sizes on the degree of smoothness of the fault representation, sometimes finding overly characteristic distributions with an excessive reduction of moderate magnitude events in some cases. Thus, this quantitative correspondence does vary some depending on model parameters. It is a behavior we can compare to observations, however, and is thus something we do want to examine. One other point regarding the distribution of sizes of events is that whereas the moderate events provide the best data constraints, the largest events contribute most to the hazard, and are thus of particular interest, but there are much fewer constraints on their long-term statistics. One robust feature of the UCERF3 modeling (Field *et al.*, 2014), and similar efforts at modeling the distribution of large events relative to the small ones on this fault system (Parsons *et al.*, 2019), have been the finding that the characteristic bump of large events in excess of the extrapolated small event rate for events on the UCERF3 faults appears to be a robust feature (Field *et al.*, 2017; Parsons *et al.*, 2019). This is certainly the case in the simulators. A fuller statistical test would be useful both in comparison of observations with the model, and in rethinking of constraints imposed on UCERF3 and potential future updates.

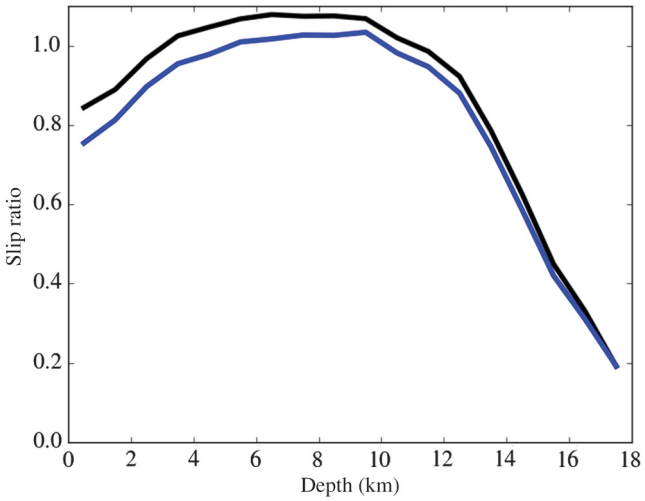

Figure 5. Depth distribution of fast coseismic slip emerging in simulation under hybrid loading conditions. Black line shows median ratio of slip rate to target slip rate. Blue line shows mean ratio. The fault system here is loaded from 2 to 14 km in depth. The shallow slip deficit is an interesting feature arising in the model that compares well with observations of coseismic slip in large earthquakes; see the Depth Distribution of Coseismic Slip section for further discussion.

Depth Distribution of Coseismic Slip

A third behavior emerging from the hybrid loaded models is the depth distribution of fast coseismic slip. Figure 5 shows median and mean slip values relative to target driving values in the model. Having values close to one at seismogenic depths indicates we are generally successfully reproducing target slip rates. The undershoot at shallow depth, in the unloaded Z_1 region, is an interesting feature. Differentials between surface and average deeper slip have been a long-standing noted and puzzling feature of geological and geodetic and seismological observations of large earthquakes (Simons *et al.*, 2002; Fialko *et al.*, 2005; Roten *et al.*, 2017), though the size of the shallow slip deficit remains a subject of active research (Xu *et al.*, 2016). Here, this feature is arising naturally from the loading, and with long-term slip deficit fractions that compare well with large event observations. One important thing to emphasize is that, as noted briefly in the opening sentence of this paragraph, we are plotting here the fast coseismic slip during earthquake events. Other slip modes can also be modeled such as creep and stable sliding, and even slow slip events (Colella *et al.*, 2013). Here, we focus our attention just on the fast coseismic slip as this is what is most relevant to earthquake shaking and hazard. If this were the only type of slip on the fault long-term slip gradients and thus strains and stresses would develop in the model. Instead, some other type of slower deformation such as afterslip and creep and bulk deformation can occur off of faults to maintain long-term steady states. Mixing of stable and unstable sliding at a given location on faults arises naturally under rate-and-state friction, and is a function of stress state (Helmstetter and Shaw, 2009). Approximations in the

model allow us to not need to explicitly model the slow processes that relieve the long-term stresses, though we could if so desired. Here, we take advantage of the fast speedup enabled by keeping track of stress transfer due just to fast coseismic sliding. This gives a tremendous numerical speedup, and an ability to focus on the part of the slip budget most relevant to earthquake events and shaking and hazard. Interestingly, it connects with long-standing geological and geodetic observations along with seismological inversions as well which have suggested shallow coseismic slip deficits relative to a deeper seismogenic layer behavior (Simons *et al.*, 2002; Fialko *et al.*, 2005; Xu *et al.*, 2016).

Discussion and Conclusions

The physical meaning and implications of the upper and lower Z_1 and Z_2 zero stressing-rate length scales are interesting questions. In the upper layer, lack of seismicity is usually ascribed to the velocity strengthening behavior in this layer (Marone *et al.*, 1991). But there are also other things going on in this layer as well, reflected in the shallow slip deficit observations (Simons *et al.*, 2002; Fialko *et al.*, 2005; Xu *et al.*, 2016). Another aspect of this layer is the modulus is generally lower than deeper layers. If plates are driven at constant displacement rates, then if strain rates are constant but modulii are not, stress rates would not be constant. Reduced modulii in shallow layers suggest reduced stress rates in shallow layers. Shallow plastic effects also contribute to reduced shallow stressing rates.

For the deeper subseismogenic length scale Z_2, again velocity strengthening is a standard explanation for the lack of nucleations initiating below the seismogenic layer. This is indeed a relevant feature. But again other physical processes may in addition be contributing to lowered stressing rates at depth. Thermally activated creep processes in the bulk may be allowing deeper nonelastic bulk deformation on loading timescales (repeat times of large events), reducing interseismic stressing rates. A nice feature of our hybrid loading approach is it does allow ruptures to penetrate deeper coseismically, below the seismogenic layer, if they choose to do so, an aspect of large earthquake behavior suggested by some seismological (Rolandone *et al.*, 2002; Shaw and Wesnousky, 2008) and geological (Lin, 2008) observations. This is in contrast with fault models in which the lower boundary of the seismogenic layer is a hard unbreakable edge, so ruptures do not have the option of penetrating deeper. Observations of slip penetrating coseismically below the seismogenic layer are ambiguous. Some authors supported it based on pseudotachylytes in mylonite layers (Lin, 2008). Dynamic models suggest it is an expected behavior (Shaw and Wesnousky, 2008; Jiang and Lapusta, 2017).

We outlined a very straightforward method of a hybrid loading method, but other modifications of this type of iterative loading can also be applied. For example, if one wanted to fit the target slip rates better in locations where it is inaccurate, multiplying fault-slip rates by averages over mid-seismogenic depth ratios of fault-slip rates relative to target slip rates can be done. These averages can be over a full fault, or more localized length scales. Another type of hybrid modeling can be used when there are not targeted slip rates, but instead remote loading is desired so faults fully self-organize their slips given their geometry. In this case, after initially running with the given remote stress loading, only the last two steps, measuring the accumulated slip and then using this empirical slip rate in backslip mode, is a useful hybrid case. In this way, a long-term steady state is still obtained by running in the final backslip mode, while the self-organizing slip distribution is still achieved. Thus, more general hybrid loading methods can be seen as one switches back and forth and combines stress loading, modifying stress loading, and backslip loading.

We presented a new type of loading condition that has a variety of useful features, and produces a number of behaviors that compare well with observations. This loading method is not limited to the specific model we apply it to, and should be useful in other modeling contexts.

Data and Resources

All data are generated from the model and are available from author upon request.

Acknowledgments

Two anonymous reviews helped improve the article. This work was supported by the W.M. Keck Foundation, by National Science Foundation (NSF) Grant EAR-1447094, by U.S. Geological Survey (USGS) Grant AABO4717, and by the Southern California Earthquake Center (SCEC) under NSF Cooperative Agreement EAR-1033462 and USGS Cooperative Agreement G12AC20038. Computational resources were provided by NSF EAR-130035, the Blue Waters National Center for Supercomputing Applications (NCSA), and Texas Advanced Computing Center (TACC).

References

Aagaard, B. T., G. Anderson, and K. W. Hudnut (2004). Dynamic rupture modeling of the transition from thrust to strike-slip motion in the 2002 Denali fault earthquake, Alaska, *Bull. Seismol. Soc. Am.* **94,** S190, doi: 10.1785/0120040614.

Andrews, D. J. (1999). Test of two methods for faulting in finite-difference calculations, *Bull. Seismol. Soc. Am.* **89,** 931.

Ben-Zion, Y., and J. R. Rice (1997). Dynamic simulations of slip on a smooth fault in an elastic solid, *J. Geophys. Res.* **102,** no. 17, 771.

Bouchon, M., and D. Streiff (1997). Propagation of a shear crack on a nonplanar fault: A method of calculation, *Bull. Seismol. Soc. Am.* **87,** 61.

Colella, H. V., J. H. Dieterich, and K. Richards-Dinger (2013). Spatial and temporal patterns of simulated slow slip events on the Cascadia megathrust, *Geophys. Res. Lett.* **40,** no. 19, 5101–5107, doi: 10.1002/grl.50984.

Cowie, P. A., and C. H. Scholz (1992). Physical explanation for the displacement length relationship of faults using a post-yield fracture-mechanics model, *J. Struct. Geol.* **14,** no. 10, 1133–1148, doi: 10.1016/0191-8141(92)90065-5.

Dalguer, L. A., and S. M. Day (2007). Staggered-grid split-node method for spontaneous rupture simulation, *J. Geophys. Res.* **112,** no. B02302, doi: 10.1029/2006JB004467.

Dawson, T. E., and R. J. Weldon (2013). UCERF3. Appendix B: Geologic-slip-rate data and geologic deformation model, *U.S. Geol. Surv. Open-File Rept. 2013-1165*.

Day, S. M., L. A. Dalguer, N. Lapusta, and Y. Liu (2005). Comparison of finite difference and boundary integral solutions to three-dimensional spontaneous rupture, *J. Geophys. Res.* **110,** no. B12307, doi: 10.1029/2005JB003813.

Dieterich, J. H., and K. B. Richards-Dinger (2010). Earthquake recurrence in simulated fault systems, *Pure Appl. Geophys.* **167,** 1087, doi: 10.1007/s00024-010-0094-0.

Fialko, Y., D. Sandwell, M. Simons, and P. Rosen (2005). Three-dimensional deformation caused by the Bam, Iran, earthquake and the origin of shallow slip deficit, *Nature* **435,** no. 7040, 295–299, doi: 10.1038/nature03425.

Field, E. H., R. J. Arrowsmith, G. P. Biasi, P. Bird, T. E. Dawson, K. R. Felzer, D. D. Jackson, K. M. Johnson, T. H. Jordan, C. Madden, *et al.* (2014). Uniform California Earthquake Rupture Forecast, version 3 (UCERF3)—The time-independent model, *Bull. Seismol. Soc. Am.* **104,** no. 3, 1122–1180, doi: 10.1785/0120130164.

Field, E. H., T. H. Jordan, M. T. Page, K. R. Milner, B. E. Shaw, T. E. Dawson, G. P. Biasi, T. Parsons, J. L. Hardebeck, A. J. Michael, *et al.* (2017). A synoptic view of the third Uniform California Earthquake Rupture Forecast (UCERF3), *Seismol. Res. Lett.* **88,** no. 5, 1259–1267, doi: 10.1785/0220170045.

Gimbutas, Z., L. Greengard, M. Barall, and T. E. Tullis (2012). On the calculation of displacement, stress, and strain induced by triangular dislocations, *Bull. Seismol. Soc. Am.* **102,** no. 6, 2776–2780, doi: 10.1785/0120120127.

Harris, R. A., and S. M. Day (1999). Dynamic 3D simulations of earthquake on en echelon fault, *Geophys. Res. Lett.* **26,** 2089.

Harris, R. A., M. Barall, R. Archuleta, E. Dunham, B. Aagaard, J. P. Ampuero, H. Bhat, V. Cruz-Atienza, L. Dalguer, P. Dawson, *et al.* (2009). The SCEC/USGS dynamic earthquake rupture code verification exercise, *Seismol. Res. Lett.* **80,** 119.

Hauksson, E., W. Yang, and P. M. Shearer (2012). Waveform relocated earthquake catalog for Southern California (1981 to June 2011), *Bull. Seismol. Soc. Am.* **102,** no. 5, 2239–2244, doi: 10.1785/0120120010.

Helmstetter, A., and B. E. Shaw (2009). Afterslip and aftershocks in the rate-and-state friction law, *J. Geophys. Res.* **114,** no. B01308, doi: 10.1029/2007JB005077.

Jiang, J., and N. Lapusta (2017). Connecting depth limits of interseismic locking, microseismicity, and large earthquakes in models of long-term fault slip, *J. Geophys. Res.* **122,** no. 8, 6491–6523, doi: 10.1002/2017JB014030.

Lapusta, N., and Y. Liu (2009). Three-dimensional boundary integral modeling of spontaneous earthquake sequences and aseismic slip, *J. Geophys. Res.* **114,** doi: 10.1029/2008JB005934.

Lin, A. M. (2008). Seismic slip in the lower crust inferred from granulite-related pseudotachylyte in the Woodroffe thrust, Central Australia, *Pure Appl. Geophys.* **165,** 215.

Mai, P., P. Spudich, and J. Boatwright (2005). Hypocenter locations in finite-source rupture models, *Bull. Seismol. Soc. Am.* **95,** no. 3, 965–980, doi: 10.1785/0120040111.

Manighetti, I., M. Campillo, C. Sammis, P. M. Mai, and G. C. P. King (2005). Evidence for self-similar, triangular slip distributions on earthquakes: Implications for earthquake and fault mechanics, *J. Geophys. Res.* **110,** no. B05302, doi: 10.1029/2004JB003174.

Marone, C., and C. H. Scholz (1988). The depth of seismic faulting and the upper transition from stable to unstable slip regimes, *Geophys. Res. Lett.* **15,** no. 6, 621–624, doi: 10.1029/GL015i006p00621.

Marone, C. J., C. H. Scholz, and R. Bilham (1991). On the mechanisms of earthquake afterslip, *J. Geophys. Res.* **96,** 8441.

Marshall, S. T., M. L. Cooke, and S. E. Owen (2008). Effects of non-planar fault topology and mechanical interaction on fault slip distributions in the Ventura Basin, California, *Bull. Seismol. Soc. Am.* **98,** 1113.

Nazareth, J. J., and E. Hauksson (2004). The seismogenic thickness of the Southern California crust, *Bull. Seismol. Soc. Am.* **94,** 940.

Parsons, T., E. Geist, R. Console, and R. Carluccio (2019). Characteristic earthquake magnitude frequency distributions on faults calculated from consensus data in California, *J. Geophys. Res.* **123,** no. 12, 10,761–10,784.

Pollitz, F. F. (2012). ViscoSim earthquake simulator, *Seismol. Res. Lett.* **83,** no. 6, 979–982, doi: 10.1785/0220120050.

Richards-Dinger, K., and J. H. Dieterich (2012). RSQSim earthquake simulator, *Seismol. Res. Lett.* **83,** no. 6, 983, doi: 10.1785/0220120105.

Robinson, R., R. Van Dissen, and N. Litchfield (2011). Using synthetic seismicity to evaluate seismic hazard in the Wellington region, New Zealand, *Geophys. J. Int.* **187,** no. 1, 510–528, doi: 10.1111/j.1365-246X.2011.05161.x.

Rolandone, F., R. Bürgmann, and R. M. Nadeau (2002). Time-dependent depth distribution of aftershocks: Implications for fault mechanics and crustal rheology, *Seismol. Res. Lett.* **73,** 229.

Roten, D., K. B. Olsen, and S. M. Day (2017). Off-fault deformations and shallow slip deficit from dynamic rupture simulations with fault zone plasticity, *Geophys. Res. Lett.* **44,** no. 15, 7733–7742, doi: 10.1002/2017GL074323.

Sachs, M. K., E. M. Heien, D. L. Turcotte, M. B. Yikilmaz, J. B. Rundle, and L. H. Kellogg (2012). Virtual California earthquake simulator, *Seismol. Res. Lett.* **83,** no. 6, 973–978, doi: 10.1785/0220120052.

Savage, J. (1983). A dislocation model of strain accumulation and release at a subduction zone, *J. Geophys. Res.* **88,** no. NB6, 4984–4996, doi: 10.1029/JB088iB06p04984.

Shaw, B. E. (2004). Self-organizing fault systems and self-organizing elastodynamic events on them: Geometry and the distribution of sizes of events, *Geophys. Res. Lett.* **31,** no. 17, 603, doi: 10.1029/2004GL019726.

Shaw, B. E., and S. G. Wesnousky (2008). Slip-length scaling in large earthquakes: The role of deep penetrating slip below the seismogenic layer, *Bull. Seismol. Soc. Am.* **98,** 1633.

Shaw, B. E., K. R. Milner, E. H. Field, K. Richards-Dinger, J. J. Gilchrist, J. H. Dieterich, and T. H. Jordan (2018). A physics-based earthquake simulator replicates seismic hazard statistics across California, *Sci. Adv.* **4,** eaau0688.

Shaw, B. E., K. Richards-Dinger, and J. H. Dieterich (2015). Deterministic model of earthquake clustering shows reduced stress drops for nearby aftershocks, *Geophys. Res. Lett.* **42,** 9231, doi: 10.1002/2015GL066082.

Simons, M., Y. Fialko, and L. Rivera (2002). Coseismic deformation from the 1999 M_w 7.1 Hector Mine, California, earthquake as inferred from InSAR and GPS observations, *Bull. Seismol. Soc. Am.* **92,** no. 4, 1390–1402, doi: 10.1785/0120000933.

Tullis, T. E., K. Richards-Dinger, M. Barall, J. H. Dieterich, E. H. Field, E. M. Heien, L. H. Kellogg, F. F. Pollitz, J. B. Rundle, M. K. Sachs, *et al.* (2012). A comparison among observations and earthquake simulator results for the allcal2 California fault model, *Seismol. Res. Lett.* **83,** no. 6, 994–1006, doi: 10.1785/0220120094.

Ward, S. (2000). San Francisco Bay area earthquake simulations: A step toward a standard physical earthquake model, *Bull. Seismol. Soc. Am.* **90,** no. 2, 370–386, doi: 10.1785/0119990026.

Ward, S. N. (2012). ALLCAL earthquake simulator, *Seismol. Res. Lett.* **83,** no. 6, 964–972, doi: 10.1785/0220120056.

Xu, X., X. Tong, D. T. Sandwell, C. W. D. Milliner, J. F. Dolan, J. Hollingsworth, S. Leprince, and F. Ayoub (2016). Refining the shallow slip deficit, *Geophys. J. Int.* **204,** no. 3, 1867–1886, doi: 10.1093/gji/ggv563.

Lamont–Doherty Earth Observatory
Columbia University
Palisades, New York 10964 U.S.A.
shaw@ldeo.columbia.edu

Manuscript received 27 April 2018;
Published Online 15 October 2019